

Crystallization Behavior and Heat Transfer of Fluorine-Free Mold Fluxes with Different Na₂O Concentration



JIAN YANG, JIANQIANG ZHANG, YASUSHI SASAKI, OLEG OSTROVSKI, CHEN ZHANG, DEXIANG CAI, and YOSHIAKI KASHIWAYA

In this study, the crystallization behavior and heat transfer of CaO-SiO₂-Na₂O-B₂O₃-TiO₂-Al₂O₃-MgO-Li₂O fluorine-free mold fluxes with different Na₂O contents (5 to 11 mass pct) were studied using single/double hot thermocouple technique (SHTT/DHTT) and infrared emitter technique (IET), respectively. Continuous cooling transformation (CCT) and time-temperature transformation (TTT) diagrams constructed using SHTT showed that crystallization temperature increased and incubation time shortened with the increase of Na₂O concentration, indicating an enhanced crystallization tendency. The crystallization process of mold fluxes in the temperature field simulating the casting condition was also investigated using DHTT. X-ray diffraction (XRD) analysis of the quenched mold fluxes showed that the dominant phase changed from CaSiO₃ to Ca₁₁Si₄B₂O₂₂ with the increasing concentration of Na₂O. The heat transfer examined by IET showed that the increase of Na₂O concentration reduced the responding heat flux when Na₂O was lower than 9 mass pct but the further increase of Na₂O to 11 mass pct enhanced the heat flux. The correlation between crystallinity and heat transfer was discussed in terms of crystallization tendency and crystal morphology.

DOI: 10.1007/s11663-016-0715-9

© The Minerals, Metals & Materials Society and ASM International 2016

I. INTRODUCTION

MOLD fluxes serve essential roles in the continuous casting of steel, such as lubrication, heat transfer control, thermal insulation, oxidation prevention, inclusion entrapment, *etc.*^[1–3] The non-uniform heat distribution on solidifying shell is likely to cause longitudinal cracks on the surface of steel products in the casting of slabs.^[4] The defects become more serious and frequent in casting medium-carbon steels which undergo δ-Fe to γ-Fe peritectic phase transformation during solidification with 4 pct volumetric shrinkage. In practice, mold fluxes with high crystallization tendency are recommended in the casting of cracking-sensitive steels since the thick crystalline flux layer formed between strand and copper mold inhibits heat transfer.^[5–7] It is generally accepted that photons are scattered by grain boundaries, which reduces the thermal radiation; heat transfer is also

impeded by pores, cracks, and air gaps formed as a consequence of the formation of crystalline flux layer.^[7–10] The suppression of heat withdrawal rate alleviates the uneven thermal stress so as to decrease the likelihood of surface imperfections. Currently, most of commercial mold fluxes contain fluorides, such as CaF₂ and NaF, to ameliorate lubricity of liquid flux layer and control heat transfer rate through the precipitation of cuspidine (Ca₄Si₂O₇F₂).^[11–14] However, the ever-rising demand for eco-friendly steel-making process requires the industry to minimize the pollutive emission of gaseous fluorides, such as HF, SiF₄, and NaF, during casting operation, which causes corrosion of the secondary cooling system of casters and the hazards to environment.^[1,15–17] Therefore, the development of fluorine-free mold fluxes has become a hotspot of research in pyrometallurgy in recent years. Although several fluorine-free substitutes for cuspidine were proposed, such as Ca₁₁Si₄B₂O₂₂,^[18–21] Ca₂Si₃Na₂O₉,^[22] and CaSiTiO₅,^[23] the lack of fundamental knowledge of fluorine-free flux system still inhibits their application.

Na₂O has been proved to be an important component that significantly affects the properties of fluorine-containing mold fluxes.^[13,14,18,24] It is considered to be an important component for the design of fluorine-free mold fluxes. In this study, the influence of Na₂O on crystallization behavior and heat transfer of CaO-SiO₂-Na₂O-B₂O₃-based fluorine-free mold fluxes is investigated using hot thermocouple technique (HTT) and infrared emitter technique (IET), respectively. The aim of this study is to build a deeper understanding of the role of Na₂O in the fluorine-free flux system.

JIAN YANG, Ph.D. Candidate, JIANQIANG ZHANG, Associate Professor, YASUSHI SASAKI, Visiting Professor, and OLEG OSTROVSKI, Emeritus Professor, are with the School of Materials Science and Engineering, University of New South Wales, Sydney, NSW, 2052, Australia. Contact e-mail: j.q.zhang@unsw.edu.au CHEN ZHANG and DEXIANG CAI, Senior Research Fellows, are with the Baosteel Group Corporation Research Institute, Shanghai, 201900, China. YOSHIAKI KASHIWAYA, Associate Professor, is with the Department of Energy Science and Technology, Kyoto University, Yoshida Honmachi, Sakyo-ku, Kyoto, 606-8501, Japan.

Manuscript submitted April 13, 2016.

Article published online June 8, 2016.

II. EXPERIMENTAL METHODS

A. Sample Preparation

In the present study, compositions of the mold fluxes were designed on the basis of thermodynamic modeling using FactSage.^[25] The fluorine-free mold fluxes were synthesized by melting pre-mixed reagent grade CaCO₃, SiO₂, Al₂O₃, B₂O₃, Na₂CO₃, TiO₂, MgO, and Li₂CO₃ at 1673 K (1400 °C) for 20 minutes in graphite crucibles. The melted fluxes were quenched onto a copper plate and then ground into powders. Chemical compositions of the amorphous fluorine-free fluxes are listed in Table I, marked as Samples 1 to 4. Two fluorine-containing industrial mold fluxes for low-carbon steel and medium-carbon steel casting, named as LC and MC, were included for comparison and their compositions are also listed in Table I. The concentrations of B₂O₃ and Li₂O were determined by inductively coupled plasma (ICP) analysis; other components were analyzed by X-ray fluoroscopy (XRF).

B. Experimental Apparatus

1. Hot thermocouple technique

The crystallization behavior of mold fluxes was determined by single hot thermocouple technique (SHTT) and double hot thermocouple technique (DHTT) developed by Kashiwaya *et al.*^[26,27] The schematic setup of SHTT/DHTT is given in Figure 1(a). A hot thermocouple could achieve a high cooling rate up to 220 K/s by manual control or 30 K/s by automatic control due to its low thermal inertia, which makes it capable of simulating the highest cooling rate that mold fluxes encounter in the infiltration process.^[26] The mold flux powders (ca. 10 mg) were mounted on a B-type thermocouple tip as presented in Figure 1(b), and heated or cooled in accordance with the programmed temperature profile in SHTT. The sample was attached between two thermocouples in DHTT as shown in Figure 1(b). The crystallization process of mold fluxes was *in situ* observed and recorded by a video camera.

2. Infrared emitter technique

The heat transfer tests were carried out using infrared emitter technique (IET) developed by Carnegie Mellon University.^[28–30] The schematic layout of IET is given in Figure 2. Infrared radiation emits from a heating lamp with a set of tungsten filaments to the flux disk. The radiation intensity was adjusted by the applied voltage in accordance with a desired power profile. The wavelength of the radiation is close to that emitted from the

solidifying strand.^[16] A mold flux disk was placed on a brass base with four thermocouples embedded under the top surface of brass base. The responding temperatures measured by the thermocouples at different depths were recorded and converted to the heat flux according to Fourier's law:^[29]

$$q = \frac{-1}{n} \sum_i k \left(\frac{dT}{dx} \right), \quad [1]$$

where q is the heat flux, n presents the number of thermocouples, k refers to the thermal conductivity of copper.

C. Experimental Procedure

1. Crystallization behavior tests

The CCT and TTT diagrams were constructed using SHTT in continuous cooling and isothermal experiments whose temperature profiles are given in Figures 3(a) and (b), respectively. In continuous cooling experiments, the sample was first heated up to 1773 K (1500 °C) and held for 3 minutes to homogenize composition and remove bubbles. Then, it was continuously cooled down to 1073 K (800 °C) with different pre-set cooling ramps. The time and temperature at which the crystallinity of mold fluxes reached 0.5 vol pct were used to construct CCT curves catering for the understanding of crystallization behavior in different cooling paths when molten fluxes infiltrate into the interfacial gap between strand and copper mold.^[27] Likewise, the sample was heated up to 1773 K (1500 °C) in isothermal experiments and rapidly quenched to different pre-set temperatures after homogenization and held isothermally at the target temperatures until crystallinity reached 100 vol pct. The times when crystallinity of mold fluxes reached 0.5 and 99 vol pct were defined as the onset and end of crystallization, which were used for the construction of TTT diagrams.

The precipitated phases at different temperatures were analyzed using X-ray diffraction (XRD). Since the samples collected from the thermocouple tip are too tiny to be precisely analyzed, 5 g amorphous sample was treated at a low temperature [1173 K (900 °C)] and a high temperature [1273 K (1000 °C)], respectively, for 20 minutes in a furnace. The phase composition of the quenched samples was then identified using XRD (PANalytical Empyrean XRD) with Cu-K α radiation. The scan was conducted in the range of 2θ from 20 deg to 70 deg with the step size of 0.026 deg.

Table I. Chemical Composition of Mold Fluxes with Different Na₂O Concentration (Mass Pct)

Sample	R	CaO	SiO ₂	Al ₂ O ₃	B ₂ O ₃	Na ₂ O	TiO ₂	MgO	Li ₂ O	F
1	1.1	40.8	37.3	3.6	6.3	5.0	4.2	2.2	1.0	0
2	1.1	39.5	35.7	3.6	6.7	7.2	4.2	2.1	1.1	0
3	1.1	38.3	34.7	3.7	6.8	8.7	4.2	2.3	1.1	0
4	1.1	37.8	34.2	3.6	6.7	11.0	4.3	2.2	1.0	0
LC ^[24]	0.9	34.5	37.5	3.0	—	12.5	—	2.5	0.5	8.5
MC	1.5	43.5	30	3.8	—	6	—	3	1.3	10

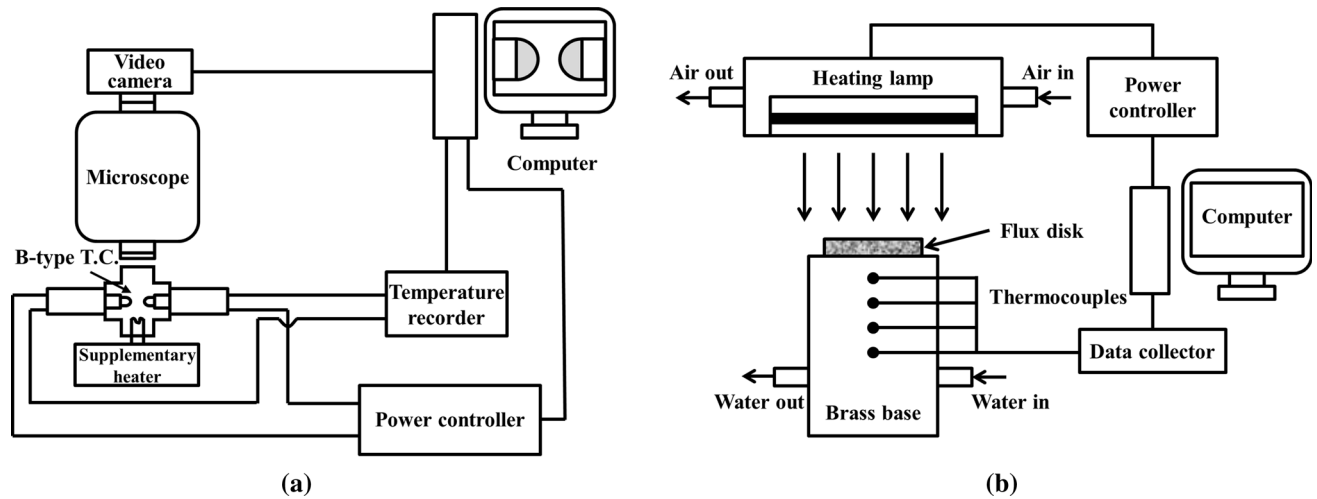


Fig. 1—Schematic representation of (a) hot thermocouple technique (HTT); (b) thermocouple setup.

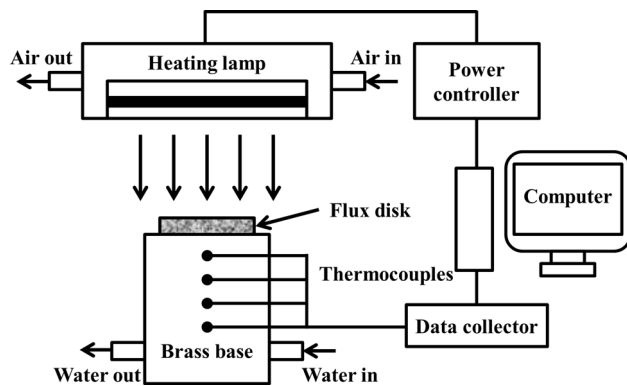


Fig. 2—Schematic representation of infrared emitter technique (IET).

Crystallization evolution of mold fluxes in a simulated thermal field was investigated in the DHTT experiments, of which the temperature profile is shown in Figure 3(c). A liquid flux film with a length of 1.5 mm was formed between two thermocouples when both of the thermocouples were heated to 1773 K (1500 °C). After holding at 1773 K (1500 °C) for 3 minutes, one thermocouple (CH-1) was quenched to 873 K (600 °C) while the other thermocouple (CH-2) was kept at 1773 K (1500 °C) to simulate the temperature gradient between solidified shell and the hot face of solid flux layer near meniscus region.^[21] Considering the buffered cooling rate when the temperature of CH-1 was approaching the target, a start point in the DHTT experiments was defined as the time at which the tangent to the cooling path and the isothermal temperature line intersected.^[21] The solidified flux films collected after DHTT experiments were used for scanning electron microscope (SEM) (Hitachi S3400) and X-ray energy dispersive spectroscopy (EDS) analyses.

2. Heat transfer tests

Heat flux across the mold flux disk was measured using IET. Mold fluxes were melted in a furnace at

1673 K (1400 °C) for homogenization and then quenched into a cylindrical copper mold with an inner diameter of 4 cm. The flux disk was removed from the mold after solidification and uploaded to another furnace in which the temperature gradually cooled down from 873 K to 573 K (600 °C to 300 °C) for normalization. Then it was ground and polished to a thickness of 4 mm. The fabricated mold flux disk was placed onto the top of the brass base, exposed to the infrared radiation. The stepwise power profile of IET tests is presented in Figure 3(d). The system emitted an increasing incident thermal radiation up to 1.6 MW/m², which is close to the radiation released from the steel strand in continuous casting.

III. RESULTS

A. Continuous Cooling Experiments

Figures 4(a) through (d) show the CCT diagrams of mold fluxes with Na₂O content varying from 5 to 11 mass pct. Three replicate measurements were conducted for the determination of crystallization temperatures at each cooling rate. For the given mold fluxes, crystallization temperature, at which the crystallinity of mold fluxes reached 0.5 vol pct, declined with increasing cooling rate. For example, the crystallization temperature of sample 1 decreased from 1368 K to 1196 K (1095 °C to 923 °C) as the cooling rate increased from 0.1 to 1 K/s. The critical cooling rate, above which crystallization was not observed during cooling process, raised from 1 to 2, 20 and 30 K/s when Na₂O content increased from 5 to 7, 9, and 11 mass pct, correspondingly. The crystallization temperature averaged out from three measurements at each cooling rate was also promoted with the increasing Na₂O content. For a fixed cooling rate of 1 K/s, the crystallization temperature increased from 1196 K (923 °C) when Na₂O was 5 mass pct to 1537 K (1264 °C) when Na₂O increased to 11 mass pct as illustrated in Figure 4(e).

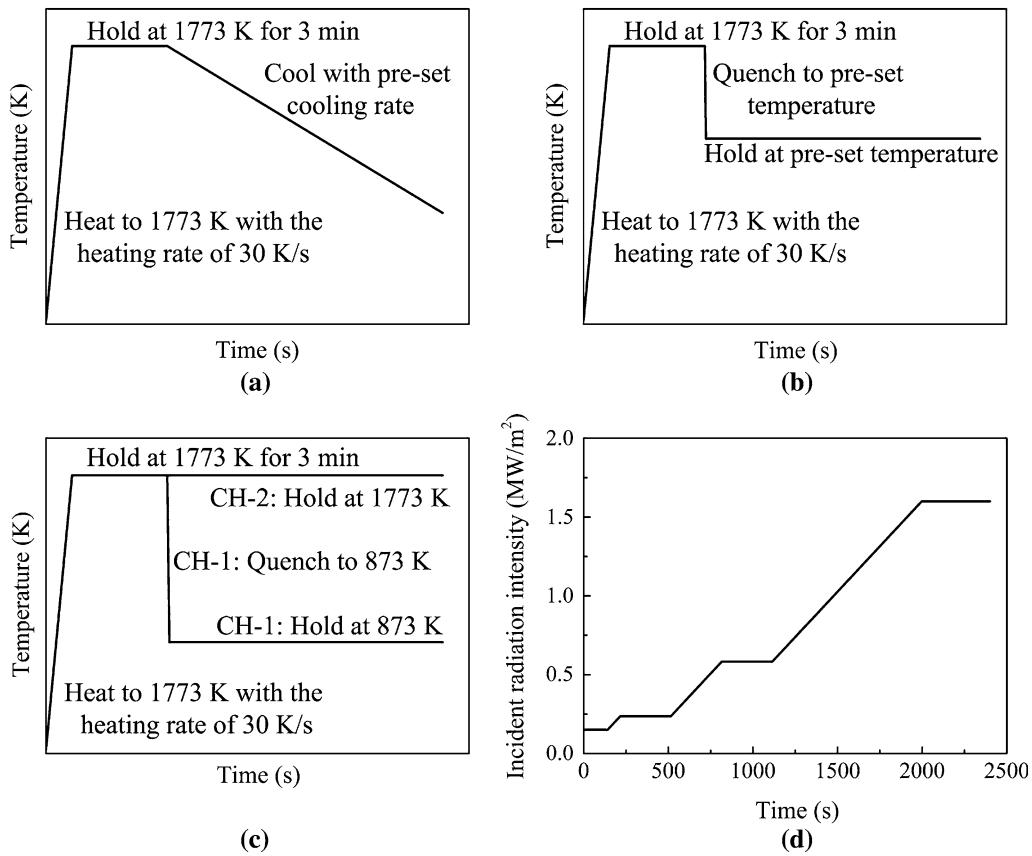


Fig. 3—Schematic temperature profiles in (a) continuous cooling experiments; (b) isothermal experiments; (c) DHTT experiments; and power profile in (d) IET tests.

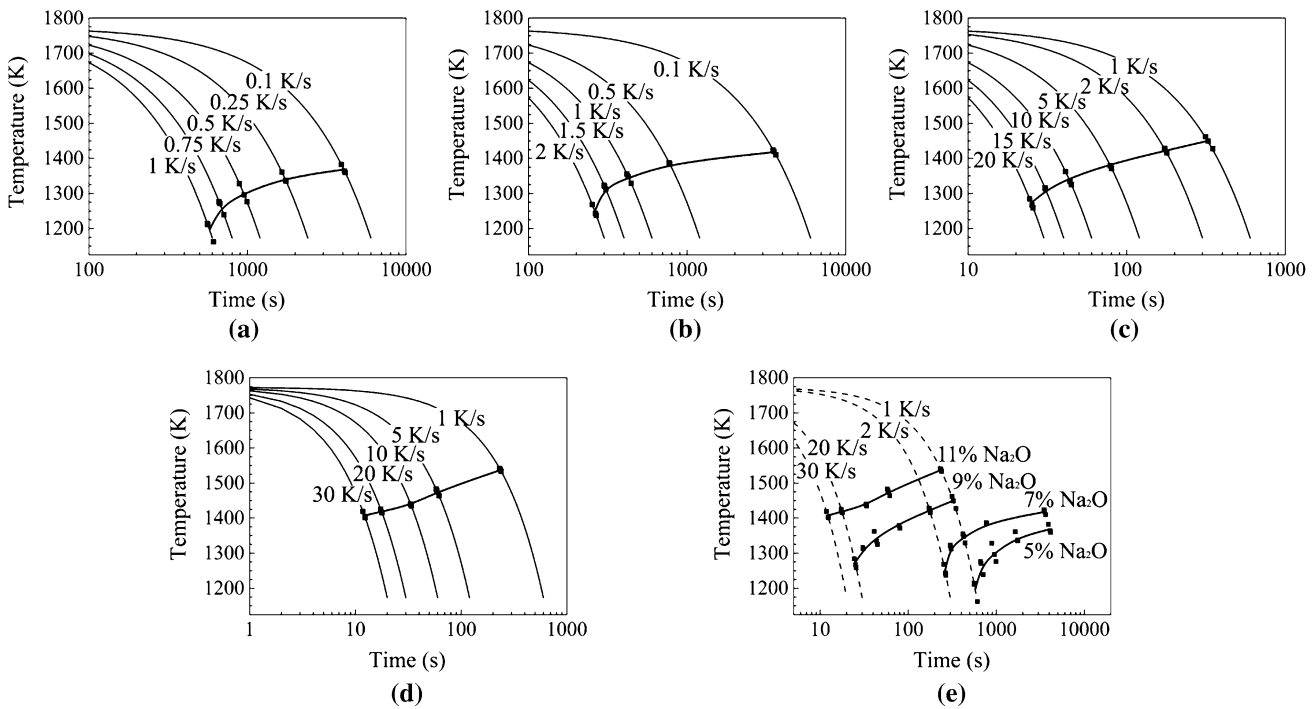


Fig. 4—CCT diagrams of mold fluxes: (a) Sample 1: $\text{Na}_2\text{O} = 5$ mass pct; (b) Sample 2: $\text{Na}_2\text{O} = 7$ mass pct; (c) Sample 3: $\text{Na}_2\text{O} = 9$ mass pct; (d) Sample 4: $\text{Na}_2\text{O} = 11$ mass pct; and (e) comparison of CCT diagrams of Sample 1 to Sample 4.

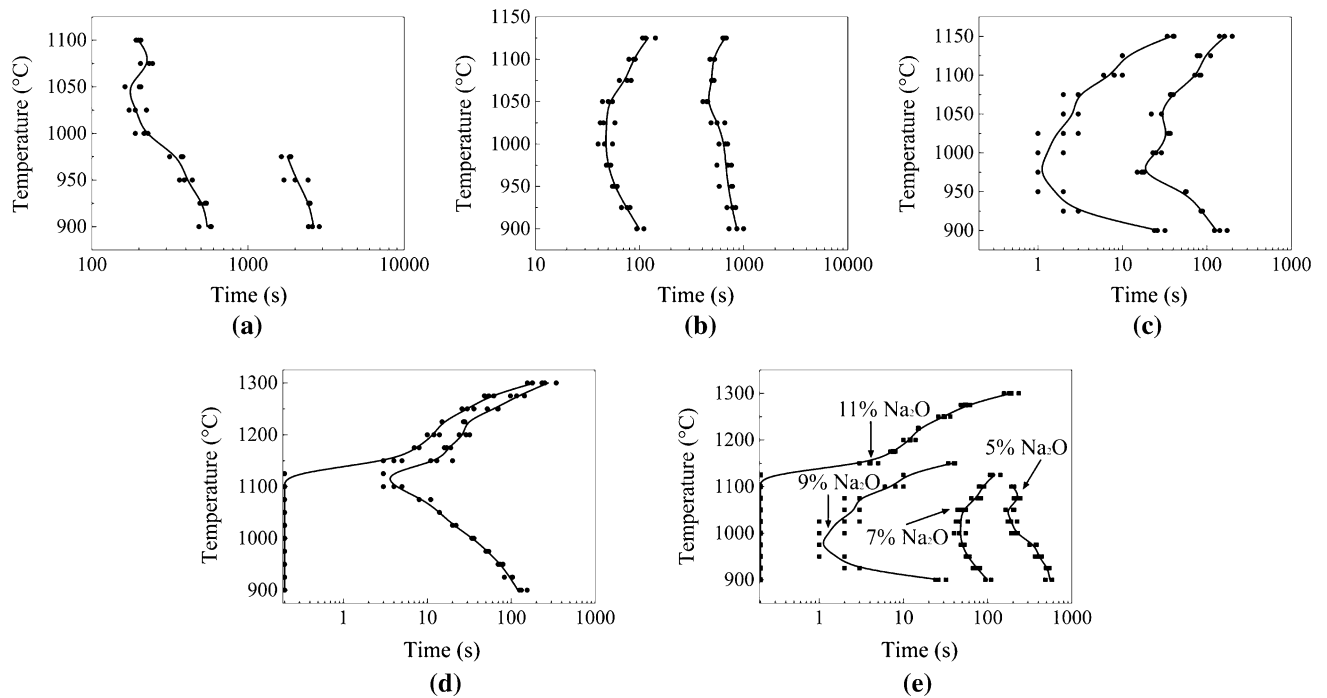


Fig. 5—TTT diagrams of mold fluxes: (a) Sample 1: Na_2O = 5 mass pct; (b) Sample 2: Na_2O = 7 mass pct; (c) Sample 3: Na_2O = 9 mass pct; (d) Sample 4: Na_2O = 11 mass pct; and (e) comparison of TTT diagrams of Sample 1 to Sample 4.

B. Isothermal Experiments

Figures 5(a) through (d) show the TTT diagrams of mold fluxes with Na_2O content ranging from 5 to 11 mass pct. Part of the end of crystallization curve of Sample 1 is not shown in Figure 5(a) since the crystals became translucent when temperature was higher than 1273 K (1000 °C), which made it difficult to determine the crystallized area when crystallization proceeded. The shortest incubation time decreased and highest crystallization temperature increased with increasing Na_2O content in fluxes, from 190 seconds and 1373 K (1100 °C) for fluxes with 5 mass pct Na_2O , to 47 seconds and 1398 K (1125 °C) for 7 mass pct Na_2O , to 1 second and 1423 K (1150 °C) for 9 mass pct Na_2O , and to almost 0 second and 1573 K (1300 °C) for 11 mass pct Na_2O as presented in Figure 5(e).

Precipitated phases of mold fluxes treated at 1173 K and 1273 K (900 °C and 1000 °C) were determined by XRD (Figure 6). As shown in Figure 6(a), the dominant phase was CaSiO_3 in the mold fluxes with 5 mass pct Na_2O at 1173 K (900 °C). Minor precipitates of $\text{Ca}_{11}\text{Si}_4\text{B}_2\text{O}_{22}$, $\text{Ca}_2\text{MgSi}_2\text{O}_7$, and CaTiO_3 were also found in the XRD patterns. The precipitation of CaSiO_3 gradually diminished as Na_2O increased and vanished when Na_2O content reached 11 mass pct; while the precipitations of $\text{Ca}_{11}\text{Si}_4\text{B}_2\text{O}_{22}$, $\text{Ca}_2\text{MgSi}_2\text{O}_7$, and CaTiO_3 were promoted as indicated in Figure 6(a). $\text{Ca}_{11}\text{Si}_4\text{B}_2\text{O}_{22}$ became the dominant phase according to its main peak height when Na_2O content was 11 mass pct. $\text{Ca}_2\text{Si}_3\text{Na}_2\text{O}_9$ was also detectable when the Na_2O content was higher than 9 mass pct. The phase composition of mold fluxes treated at 1273 K (1000 °C) is shown in Figure 6(b). The dominant precipitate was

also CaSiO_3 in the mold fluxes with low concentration of Na_2O at 1273 K (1000 °C). The variations of $\text{Ca}_{11}\text{Si}_4\text{B}_2\text{O}_{22}$, CaTiO_3 , and $\text{Ca}_2\text{Si}_3\text{Na}_2\text{O}_9$ with the increase of Na_2O were similar to the case at 1173 K (900 °C). However, $\text{Ca}_2\text{MgSi}_2\text{O}_7$ was not observed in all the samples treated at 1273 K (1000 °C) and $\text{Ca}_2\text{Si}_3\text{Na}_2\text{O}_9$ only existed in Sample 4.

C. Double Hot Thermocouple Experiments

The crystallinity evolution of mold fluxes with different content of Na_2O in a simulated thermal field is given in Figure 7. Figures 7(a1) through (a4) show the crystallization behavior of Sample 1 (5 mass pct Na_2O) under a temperature gradient of 1773 K to 873 K (1500 °C to 600 °C). Some small spherical crystals were formed between 900 to 1200 seconds, and built a clear crystalline layer at 1200 seconds. The crystalline layer further developed to both high and low temperature regions. Sample 2 started crystallization much earlier than Sample 1 as a number of nuclei were developed in the middle of the flux film before 300 seconds as shown in Figure 7(b1). Crystals grew rapidly and formed a distinct crystalline layer after 600 seconds. Sample 3 started crystallization as soon as CH-1 reached the isothermal stage. Crystals started to precipitate prior to 10 seconds and propagated to low temperature much faster than the preceding two cases as shown in Figure 7(c1). Crystallization reached a relatively stable state with a thick crystalline layer before 300 seconds. Crystallization of Sample 4 occurred even before it reached the isothermal stage. But unlike the small primarily precipitated crystals in Samples 1 to 3, the

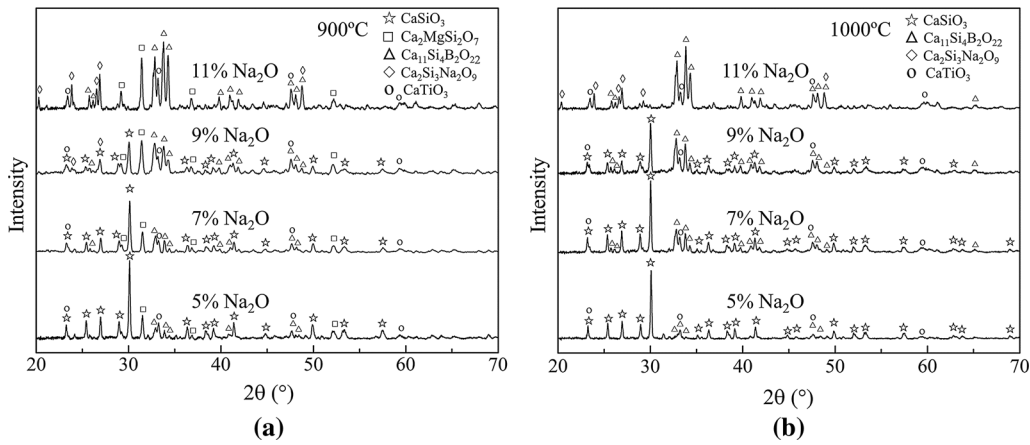


Fig. 6—XRD patterns of mold fluxes with different Na₂O content treated at (a) 1173 K (900 °C) and (b) 1273 K (1000 °C).^[31] (Copyright 2016 by The Minerals, Metals & Materials Society. Reprinted with permission.).

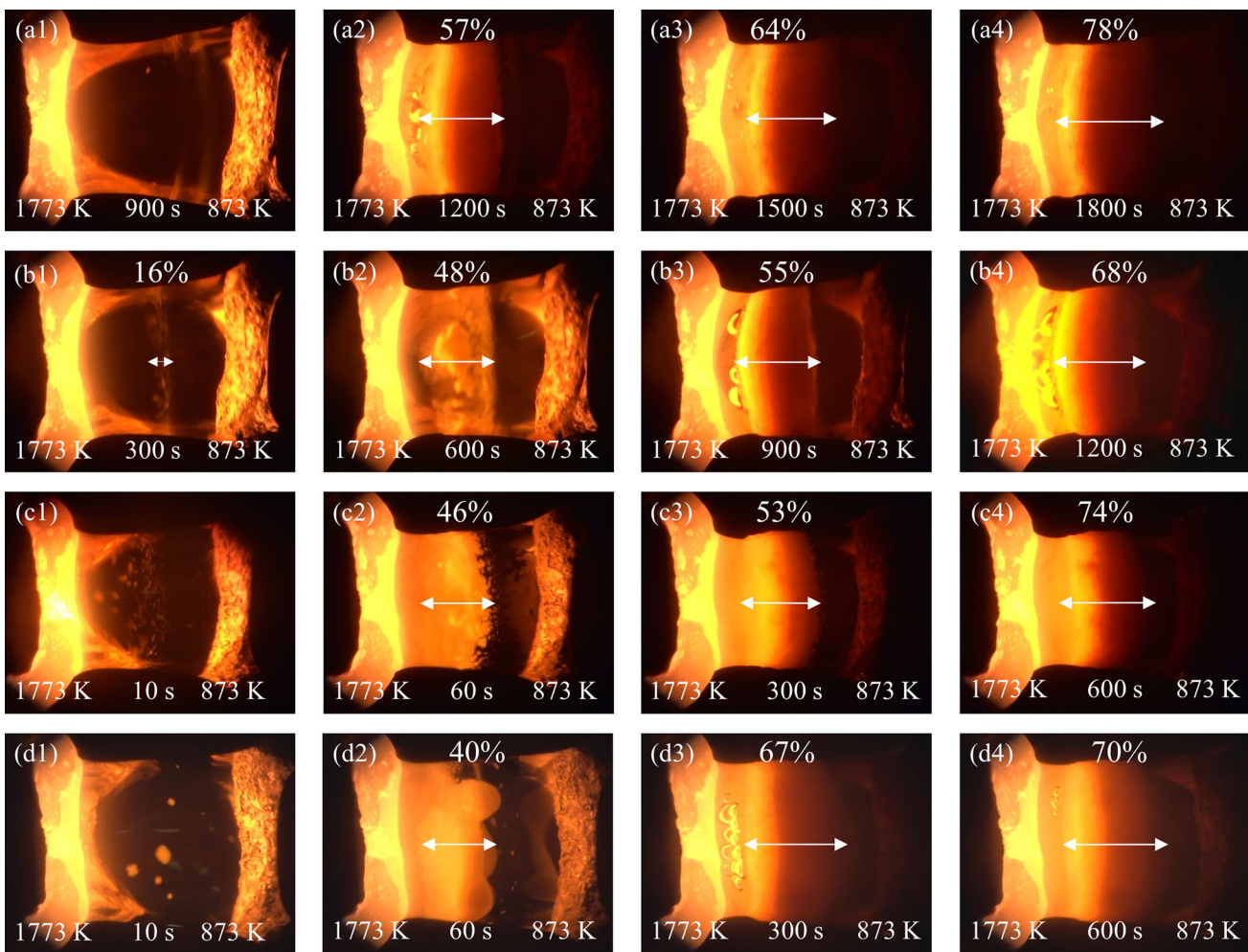


Fig. 7—Crystallization process of mold fluxes in DHTT experiments: (a1) to (a4): Sample 1 at 900 s, 1200 s, 1500 s and 1800 s; (b1) to (b4): Sample 2 at 300, 600, 900, and 1200 s; (c1) to (c4): Sample 3 at 10, 60, 300, and 600 s; (d1) to (d4): Sample 4 at 10, 60, 300, and 600 s.

large equiaxed crystals were formed in Sample 4 as shown in Figure 7(d1). These crystals had high mobility and spread to low temperature side promptly. Some of

the equiaxed crystals formed in the liquid layer and the weak part of the crystalline layer torn apart from the crystalline layer were driven to the high temperature

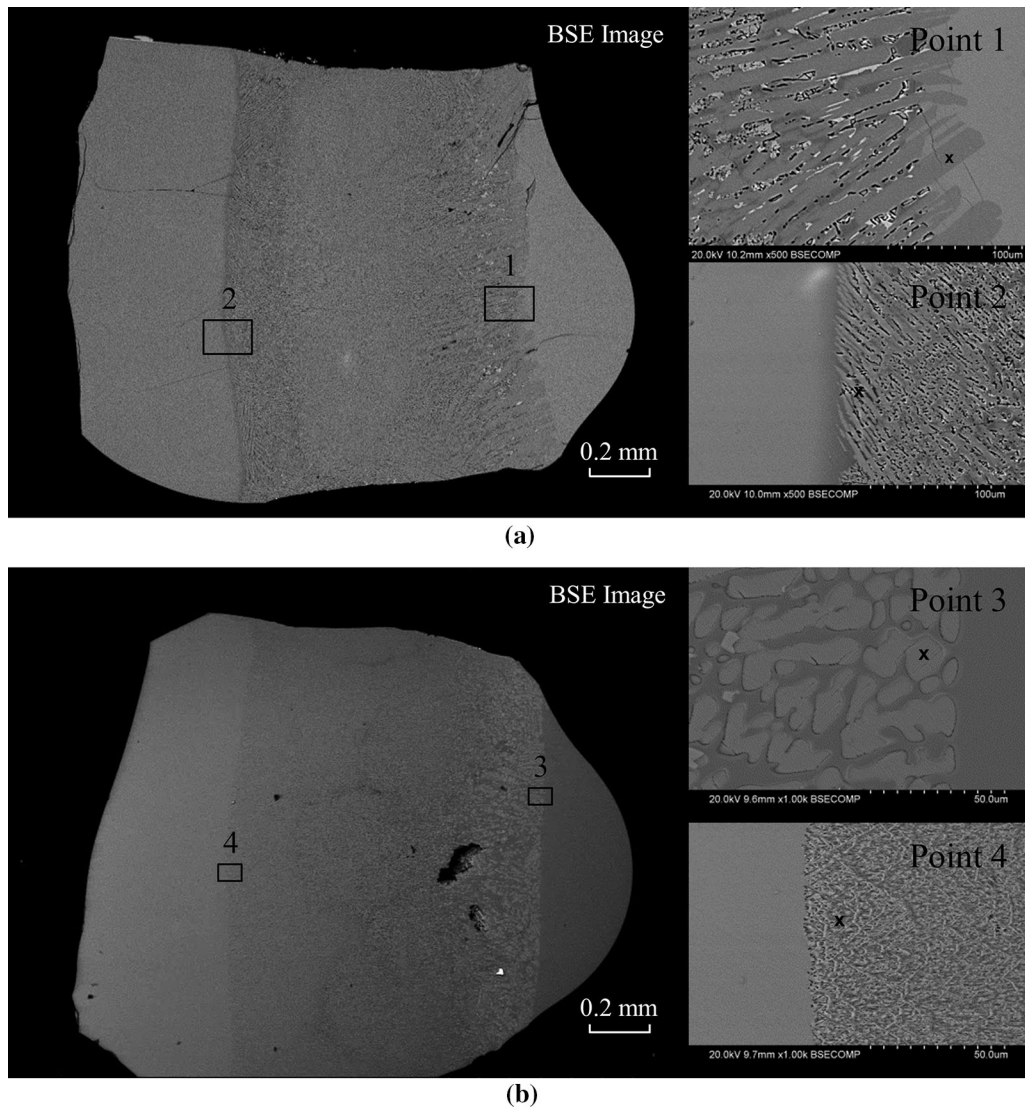


Fig. 8—Microstructure of flux films of (a) Sample 1 and (b) Sample 4 after DHTT experiments.

Table II. Normalized Concentrations of the Elements Detected by EDS (At. Pct)

Point	Ca	Si	Al	Na	Mg	Ti	O
Point 1	21.5	19.0	—	—	—	—	59.5
Point 2	21.9	16.8	0.8	—	—	1.3	59.2
Point 3	32.9	11.4	—	—	—	—	55.7
Point 4	20.6	13.8	1.7	4.0	1.5	1.4	57.0

region by Marangoni convection flow and finally melted. The flux films all exhibited a three-layer structure—liquid, crystalline, and glassy layers when crystallization proceeded to a steady stage.

The SEM–BSE images of Samples 1 and 4 are shown in Figure 8. The normalized elemental compositions of specific crystals detected by EDS are listed in Table II. Both flux films were divided into three parts distinctively. The crystalline layer was in the center of the flux

film between two glassy layers. The glassy layer on the left side remained in glassy state after CH-1 was quenched to 873 K (600 °C) during DHTT experiments; while the glassy layer on the right side was actually liquid layer in DHTT experiments, corresponding to the high temperature side of DHTT. It shrank to a hemisphere due to the surface tension as soon as the high temperature side was quenched to room temperature once the experiment ended. The crystal morphology

in two samples was different. Figure 8(a) shows that the crystals growing on the crystalline/liquid interface of Sample 1 were with a lath-shaped structure rooted firmly in the crystalline layer. According to the EDS analysis (Table II), the ratio of Ca:Si:O was approximately 1:1:3 which indicated that the phase was CaSiO_3 (wollastonite). Parallel acicular crystals were observed at the glass/crystalline interface, growing one-dimensionally along the heat transfer direction as shown by Zhou *et al.* in their DHTT thermal field simulation.^[32] But the elemental composition of the crystal did not clearly match to any single phase. It was possibly because the spatial resolution of X-ray beam in EDS analysis was not sufficiently high to strictly constrain X-ray beam within the acicular crystal and therefore the elements of the vicinal glassy phase were also detected. Figure 8(b) shows that the large crystals were randomly distributed in the high temperature side of Sample 4. Some of the crystals were of equiaxed structure; the others seemed to be torn apart from the crystalline layer caused by Marangoni convection flow in DHTT experiments of Sample 4. The phase might be $\text{Ca}_{11}\text{Si}_4\text{B}_2\text{O}_{22}$ according to the Ca/Si ratio detected by EDS and XRD results (Figure 6) as EDS could not confirm the presence of boron which is too light to be detected. The crystals in

the low temperature side of crystalline layer presented a mash-like morphology whose composition was not confirmed due to the complexity of fine precipitates in this region.

D. Heat Transfer Tests

The flux disk evolution of Sample 1 under infrared radiation is shown in Figure 9. Along with the increase of incident radiation intensity, the top of disk surface became opaque when crystallization occurred and gradually propagated to the bottom side. Then, the upper part of the flux disk started to melt and form a hemisphere layer at high temperature. After the heat transfer test, the flux disk was taken off the brass base. The side view of the flux disk exhibited a thin glassy layer on its top surface which was formed as the melted flux solidified into the glassy state after experiment. The cross-sectional view indicated that the bottom of the flux disk was also in glassy state. But unlike the glassy layer on the top surface of the flux disk, the bottom remained glassy state throughout the experiment due to its low temperature. The middle part of the flux disk was opaque as a result of crystallization. It was consistent with what was expected in the DHTT experiments, in which flux films all exhibited a three-layer structure, including liquid, crystalline, and glassy layers. The calculated heat fluxes through the mold flux disks are given in Figure 10. As the incident radiation increased, the responding heat flux increased accordingly. As seen in Figure 10(a), the average responding heat flux at the incident radiation of 1.6 MW/m^2 dropped from 743 ± 4.6 , 677 ± 7.4 , to $595 \pm 5.0 \text{ kW/m}^2$ with increasing Na_2O content from 5 to 7 and 9 mass pct, but a further increase of Na_2O content to 11 mass pct increased the heat transfer rate to $641 \pm 5.0 \text{ kW/m}^2$. Comparing the heat flux of the fluoride-free mold fluxes with industrial mold fluxes under the same incident radiation intensity (Figure 10(b)), the responding heat flux of Sample 3 (9 mass pct Na_2O) was closest to that of the fluoride-containing industrial mold fluxes as the heat fluxes of LC and MC powders were 558 ± 12.7 and $540 \pm 6.1 \text{ kW/m}^2$, respectively.

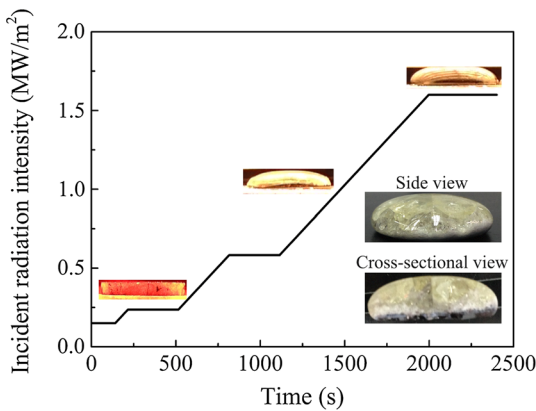


Fig. 9—Flux disk evolution of Sample 1 under infrared radiation.

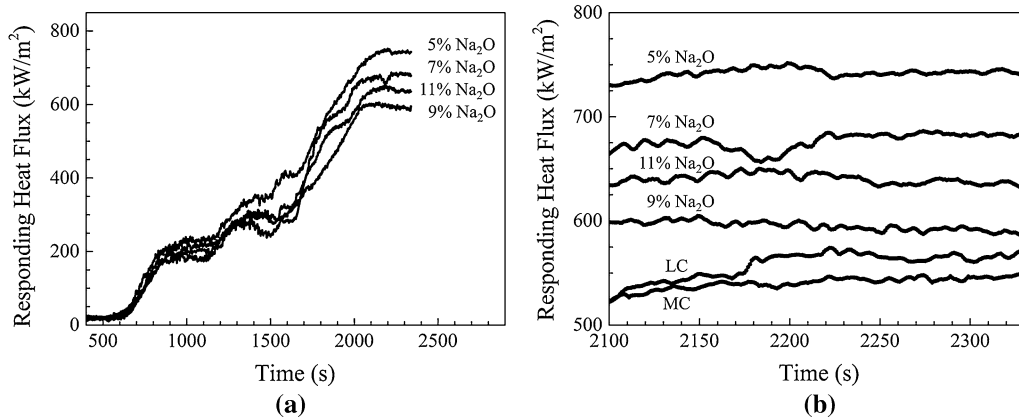


Fig. 10—(a) Heat flux of mold fluxes; (b) Comparison of the heat flux of fluoride-free mold fluxes and industrial fluxes under the incident radiation of 1.6 MW/m^2 .^[31] (Copyright 2016 by The Minerals, Metals & Materials Society. Reprinted with permission.)

IV. DISCUSSION

A. Effect of Na_2O on the Structure and Crystallization Behavior of Mold Fluxes

Silicate melts are normally described using the tetrahedral SiO_4^{4-} network model. The roles of the cations in the melts depend on their size and polarisability. According to the network theory extended by Dietzel,^[31]

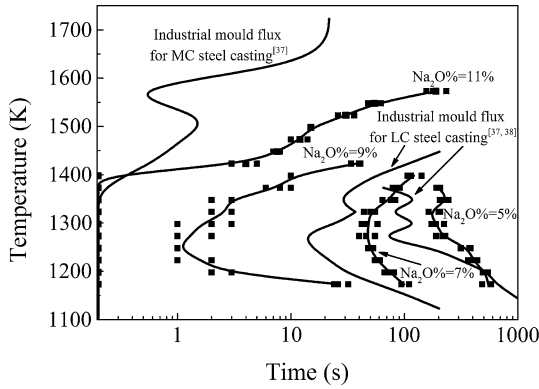


Fig. 11—Comparison of onset of crystallization in TTT diagrams of fluorine-free mold fluxes and commercial mold fluxes.

the interaction between a cation and an oxygen anion can be characterized by the field strength, F , as follows:

$$F = Z_c/a^2, \quad [2]$$

where Z_c is the valency of cation and a is the sum of the radii of the cation and oxygen anion. The cations whose field strengths range from 0.1 to 0.4 are classified as network modifiers that intrinsically break Si-O bond due to their strong attraction force toward oxygen anions.^[33] Since the field strength of Na^+ is 0.19, the addition of Na_2O is expected to break Si-O bonds in SiO_4^{4-} tetrahedral network as a network modifier, forming non-bridging oxygens (NBOs) in silicate melts. As the mobility of ions is promoted in such depolymerized melts, it reduces the initial viscosity of flux melts and consequently affects the kinetic barrier for nucleation and crystal growth. Nucleation rate I is calculated using the following equation:^[34]

$$I = \frac{Ah}{3\pi\lambda^3\eta} \exp\left(\frac{W^*}{kT}\right), \quad [3]$$

where A is the pre-exponential factor, W^* is the thermodynamic free energy barrier for nucleation, k is the Boltzmann constant, T is the absolute temperature, h is Planck constant, λ represents the atomic jump

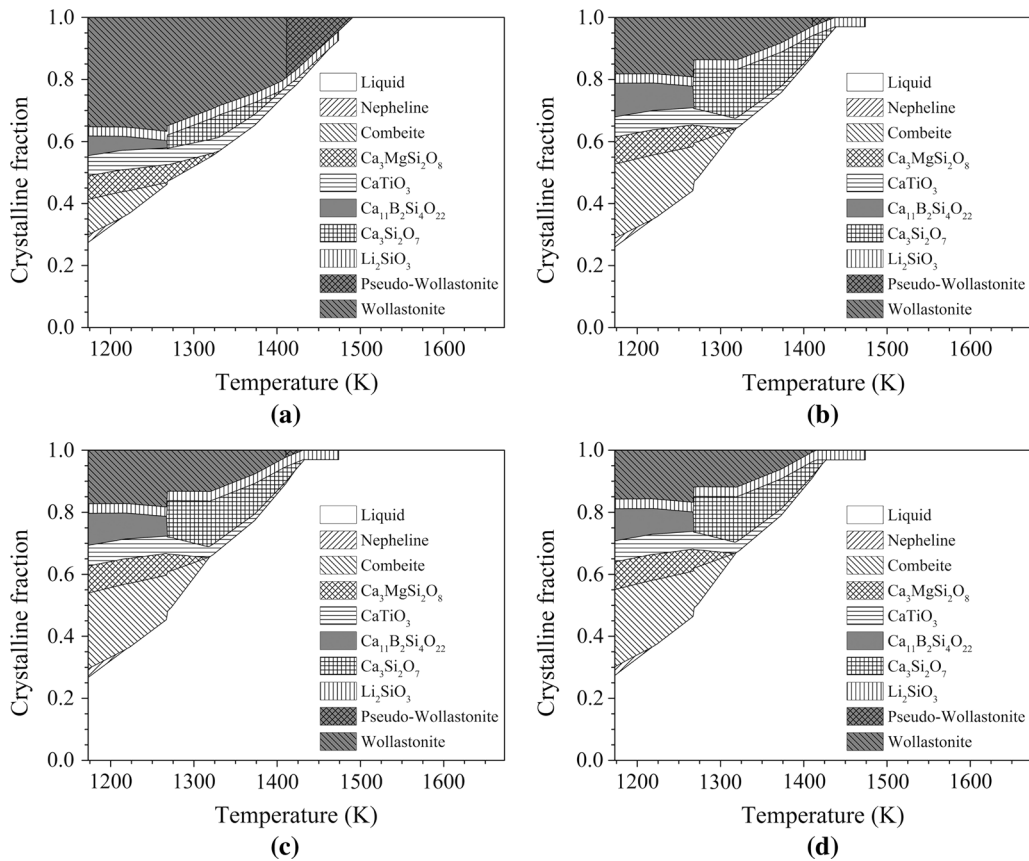


Fig. 12—Crystallinity evolution of mold fluxes calculated by FactSage 7.0: (a) Sample 1 (5 mass pct Na_2O); (b) Sample 2 (7 mass pct Na_2O); (c) Sample 3 (9 mass pct Na_2O); and (d) Sample 4 (11 mass pct Na_2O).

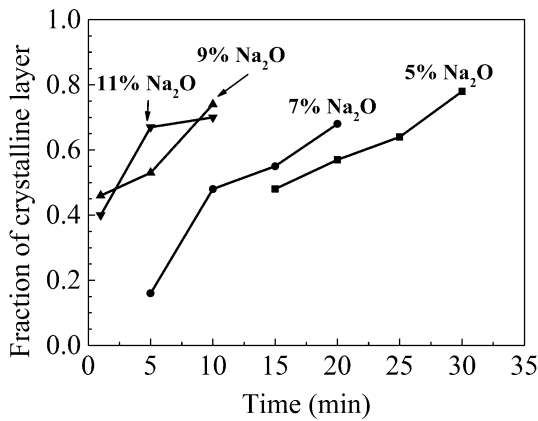


Fig. 13—Crystallinity evolution in DHTT experiments.^[31] (Copyright 2016 by The Minerals, Metals & Materials Society. Reprinted with permission.)

distance, and η is the viscosity. Likewise, the growth rate of crystals U is given by:^[34]

$$U = \frac{kT}{3\pi a_a^2 \eta} \left[1 - \exp\left(\frac{\Delta G}{kT}\right) \right], \quad [4]$$

where a_a is the interatomic separation distance, ΔG is the thermodynamic barrier for crystal growth. Therefore, the increase of Na₂O content accelerates the nucleation and crystal growth in flux melts. Phenomenally, it raised critical cooling rate and shortened the incubation time in continuous cooling and isothermal experiments as confirmed by the CCT and TTT diagrams of mold fluxes (Figures 4 and 5), indicating an enhanced crystallization tendency of mold fluxes. This promotion effect became especially significant when Na₂O content increased from 7 to 9 mass pct as the critical cooling rate raised from 2 to 20 K/s and the shortest incubation time decreased from 47 to 1 seconds. Compared with fluorine-containing mold fluxes,^[18,35] it seems that the role of Na₂O as a network modifier was not affected by fluorides.

Since the maximal cooling rate in the meniscus zone is estimated to be 20 K/s during continuous casting operation,^[26,36] Samples 3 and 4 are expected to precipitate crystals directly from the molten state. It makes them favorable in casting cracking-sensitive steel which requires heat transfer suppression once the strand starts solidification. Figure 11 presents the comparison of the TTT diagrams of fluorine-free mold fluxes and commercial fluxes reported in literature.^[37,38] It confirms that Sample 4 (11 mass pct Na₂O) showed a similar shortest incubation time to that of industrial mold fluxes for medium-carbon steel casting; while the crystallization behavior of Sample 2 (7 mass pct Na₂O) is similar to that of commercial mold fluxes for low-carbon steel casting.

B. Precipitated Phases in the Process of Flux Solidification

XRD analyses of quenched samples (Figure 6) demonstrated that their mineralogical composition was dependent upon temperature and chemical composition.

Compounds, Ca₁₁Si₄B₂O₂₂ and Ca₂Si₃Na₂O₉, detected by the XRD analyses are promising substitutes for cuspidine according to the literature.^[18–22] The precipitate of Ca₁₁Si₄B₂O₂₂ was the major phase in mold fluxes with 11 mass pct Na₂O. It has a similar melting temperature to cuspidine^[18,39,40] as well as appropriate thermal resistance and crystallization tendency.^[18–21] According to both the crystallization behavior tests and XRD analyses, the precipitation of Ca₁₁Si₄B₂O₂₂ facilitated crystallization of mold fluxes. At high concentration of Na₂O, Ca₂Si₃Na₂O₉ was also formed which was reported to promote the lubricity of fluorine-free mold fluxes.^[22] The precipitation of Ca₂MgSi₂O₇ was sensitive to the annealing temperature. The increase of temperature strongly inhibited its precipitation as Ca₂MgSi₂O₇ vanished when the temperature raised from 1173 K to 1273 K (900 °C to 1000 °C).

The equilibrium phases of mold fluxes at the temperature ranging from 1173 K to 1673 K (900 °C to 1400 °C) were calculated using FactSage 7.0. Results of the thermodynamic calculations are presented in Figure 12. The predicted major phase of Sample 1 was CaSiO₃ (wollastonite) which underwent a solid-state phase transformation to pseudo-wollastonite at high temperatures. It was consistent with the major precipitated phase revealed in the XRD analysis (Figure 6). Moreover, pseudo-wollastonite was reported to be a transparent phase which was difficult to be located.^[41] It could account for the fact that the crystalline of Sample 1 became translucent when crystals stretched out over 1273 K (1000 °C). The precipitation of other minor phases possibly made the flux not completely transparent. Minor precipitates of Ca₁₁Si₄B₂O₂₂, CaTiO₃, and Ca₃MgSi₂O₈ were expected to form in Sample 1. Results of the thermodynamic calculations were consistent with the precipitated phases detected using XRD although Ca₂MgSi₂O₇ was slightly different from the Mg-containing phase, Ca₃MgSi₂O₈, predicted by FactSage. Meanwhile, minor Ca₂Si₃Na₂O₉ (combeite) was also calculated to exist in Sample 1 (Figure 12(a)) but it was absent in XRD analysis of Sample 1. It could result from the limitation of the XRD analysis as the minor phase with a concentration lower than 3 mass pct may not be detectable. As shown in Figures 12(a) through (d), the fraction of CaSiO₃ gradually decreased, whereas the ratios of Ca₁₁Si₄B₂O₂₂ and Ca₂Si₃Na₂O₉ increased with the increasing amount of Na₂O but it did not have apparent effect on the precipitation of CaTiO₃ and Ca₃MgSi₂O₈. The calculated variation tendencies of the precipitations of CaSiO₃, Ca₁₁Si₄B₂O₂₂, and Ca₂Si₃Na₂O₉ were in line with those reflected in the XRD patterns, while the calculation did not confirm the predicted tendencies in the precipitation of CaTiO₃ and Ca₂Si₃Na₂O₉ in the XRD analyses. The inconsistencies between the results of the XRD analyses and the calculated phases might result from the fact that the thermodynamic calculation using FactSage simulated the equilibrium phases, while the crystallization of mold fluxes occurred under non-equilibrium conditions in the bench tests. The chemistry change in the liquid caused by segregation would affect the solidification of melts and therefore the precipitated phases might differ from

those expected in the phase diagram.^[5] The predicted phase Li_2SiO_3 with high melting temperature in the phase diagrams should not be considered since the thermodynamic information of lithium-containing compounds has not been fully included in the current database.

C. The Relationship Between Crystallization and Heat Transfer of Mold Fluxes

It is well-known that the increase of crystallization tendency of mold fluxes normally retards the heat transfer across flux films since pores, cracks, and grain boundaries scatter the radiative heat transfer.^[5-7] Therefore, the responding heat flux measured using IET was expected to reduce with the addition of Na_2O . Figure 10(a) shows that the heat flux decreased with increasing Na_2O content only when it was lower than 9 mass pct, but a further addition of Na_2O , however, slightly increased the heat flux across the flux disk. It may result from the differences in the morphology of crystals and the thermophysical properties of crystals. Figure 4 indicates that the promotion of crystallization tendency became less significant when $\text{Na}_2\text{O} \geq 9$ mass pct as the critical cooling rate only increased from 20 to 30 K/s when Na_2O content raised from 9 to 11 mass pct. But the large equiaxed crystals emerging in the vicinity of liquid/crystalline interface of Sample 4 had a relatively high mobility (Figure 8(a)) and could be easily driven by Marangoni flow. Therefore, the newly formed crystals could hardly grow from the liquid/crystalline interface, which made the formation of a stable crystalline layer difficult in the initial solidification stage. Figure 13 shows the fraction of crystalline layer measured in the DHTT experiments. The crystallinity evolution of the flux with 9 mass pct Na_2O (Sample 3) was similar to that of 11 mass pct Na_2O (Sample 4), which implied that the difference of Na_2O content in these two samples did not make a distinct difference to the crystallization rate in the simulated thermal field. In the beginning of crystallization, the ratio of crystalline layer in Sample 4 was even somewhat lower than that in Sample 3, probably because stable growth of crystalline phase in Sample 4 was impeded by a strong convection flow in the first few minutes compared with Sample 3. Therefore, the heat transfer rate may not further decrease when Na_2O content increased from 9 to 11 mass pct.

It is also possible that the different phases precipitated in the experiments presented different thermophysical properties, like thermal conductivity. The XRD analysis (Figure 6) reveals that the amounts of $\text{Ca}_{11}\text{Si}_4\text{B}_2\text{O}_{22}$ and $\text{Ca}_2\text{MgSi}_2\text{O}_7$ increased and the fraction of CaSiO_3 decreased with the increase of Na_2O content. Therefore, it is expected that the superposition of these variations should result in a monotonic change in heat transfer rate. The unexpected increase of heat transfer with the increasing Na_2O content from 9 to 11 mass pct may attribute to the precipitation of the new phase, $\text{Ca}_2\text{Si}_3\text{Na}_2\text{O}_9$, in the fluxes with high Na_2O content. The mold fluxes with major precipitate of $\text{Ca}_2\text{Si}_3\text{Na}_2\text{O}_9$ had been proved to have sound lubricity; however, they

seem to slightly promote heat transfer compared with conventional mold powders.^[22]

V. CONCLUSIONS

The crystallization behavior and heat transfer of mold fluxes of the $\text{CaO-SiO}_2\text{-Na}_2\text{O-B}_2\text{O}_3\text{-TiO}_2\text{-Al}_2\text{O}_3\text{-MgO-Li}_2\text{O}$ system with different Na_2O content were investigated using SHTT, DHTT, XRD, SEM, and IET. The major findings of this study are summarized below:

- (1) CCT and TTT diagrams indicate that the increase of Na_2O content raised the critical cooling rate and shortened the incubation time of mold fluxes. It can be concluded that the addition of Na_2O promoted the crystallization tendency of mold fluxes;
- (2) XRD results show that with the increasing amount of Na_2O , the dominant phase changed from CaSiO_3 to $\text{Ca}_{11}\text{Si}_4\text{B}_2\text{O}_{22}$. $\text{Ca}_2\text{MgSi}_2\text{O}_7$ was a major phase in the mold fluxes with high Na_2O content at 1173 K (900 °C) but it was not observed at 1273 K (1000 °C). Minor precipitates of $\text{Ca}_2\text{Si}_3\text{Na}_2\text{O}_9$ formed in the mold fluxes with high concentration of Na_2O ;
- (3) DHTT experiments revealed the crystallization evolution of mold fluxes in a thermal field simulating the temperature gradient between copper mold and strand. Liquid, glass, and crystalline layers were observed in the solidification process. The mold fluxes with high concentration of Na_2O crystallized directly from liquid fluxes and formed a crystalline phase within a short time. The microstructure of the flux films showed that the morphology of crystalline varied with temperature and concentration of Na_2O ;
- (4) Heat transfer tests revealed that Sample 3 with 9 mass pct Na_2O had the lowest responding heat flux of 595 MW/m^2 among all the fluorine-free mold fluxes, which was closest to the fluorine-containing fluxes. Although sample 4 (11 mass pct Na_2O) has higher crystallization tendency, its thermal resistance was lower than that of Sample 3 possibly due to the high mobility of large equiaxed crystals formed at high temperature region or different thermophysical properties of the precipitated phases.

ACKNOWLEDGMENTS

Financial support by Baosteel through the Baosteel-Australia Joint Research Centre, Abel Metal Services, and Australian Research Council (ARC Linkage Project LP130100773) is gratefully acknowledged.

REFERENCES

1. A. Fox, K. Mills, D. Lever, C. Bezerra, C. Valadares, I. Unamuno, J. Larauogoitia, and J. Gisby: *ISIJ Int.*, 2005, vol. 45, pp. 1051–8.
2. K. Mills and A. Fox: *ISIJ Int.*, 2003, vol. 43, pp. 1479–86.

3. J.W. Cho, H. Shibata, and J. Non-Cryst: *Solids*, 2001, vol. 282, pp. 110–7.
4. J. Brimacombe and K. Sorimachi: *Metall. Trans. B*, 1977, vol. 8B, pp. 489–505.
5. A.W. Cramb: *ISIJ Int.*, 2014, vol. 54, pp. 2665–71.
6. M. Kawamoto, Y. Tsukaguchi, N. Nishida, T. Kanazawa, and S. Hiraki: *ISIJ Int.*, 1997, vol. 37, pp. 134–9.
7. H. Nakada, M. Susa, Y. Seko, M. Hayashi, and K. Nagata: *ISIJ Int.*, 2008, vol. 48, pp. 446–53.
8. K. Tsutsumi, T. Nagasaka, and M. Hino: *ISIJ Int.*, 1999, vol. 39, pp. 1150–59.
9. M. Susa, K. Nagata, and K. Mills: *Ironmak. Steelmak.*, 1993, vol. 20, pp. 372–8.
10. W. Wang, K. Gu, L. Zhou, F. Ma, I. Sohn, D.J. Min, H. Matsuura, and F. Tsukihashi: *ISIJ Int.*, 2011, vol. 51, pp. 1838–45.
11. M. Susa, A. Kushimoto, R. Endo, and Y. Kobayashi: *ISIJ Int.*, 2011, vol. 51, pp. 1587–96.
12. T. Watanabe, H. Fukuyama, and K. Nagata: *ISIJ Int.*, 2002, vol. 42, pp. 489–97.
13. M. Hanao, M. Kawamoto, and T. Watanabe: *ISIJ Int.*, 2004, vol. 44, pp. 827–835.
14. M. Hayashi, T. Watanabe, H. Nakada, and K. Nagata: *ISIJ Int.*, 2006, vol. 46, pp. 1805–9.
15. G. Wen, S. Sridhar, P. Tang, X. Qi, and Y. Liu: *ISIJ Int.*, 2007, vol. 47, pp. 1117–25.
16. B. Lu, W. Wang, J. Li, H. Zhao, and D. Huang: *Metall. Mater. Trans. B*, 2013, vol. 44, pp. 365–77.
17. S.-Y. Choi, D.-H. Lee, D.-W. Shin, S.-Y. Choi, J.-W. Cho, and J.-M. Park: *J. Non-Cryst. Solids*, 2004, vol. 345, pp. 157–60.
18. J. Wei, W. Wang, L. Zhou, D. Huang, H. Zhao, and F. Ma: *Metall. Mater. Trans. B*, 2014, vol. 45, pp. 643–52.
19. L. Zhou, W. Wang, J. Wei, and K. Zhou: *ISIJ Int.*, 2015, vol. 55, pp. 821–9.
20. L. Zhou, W. Wang, and K. Zhou: *ISIJ Int.*, 2015, vol. 55, pp. 1916–1924.
21. J. Yang, J. Zhang, Y. Sasaki, O. Ostrovski, C. Zhang, D. Cai, and Y. Kashiwaya: *ISIJ Int.*, 2016, vol. 56, pp. 574–83.
22. N. Takahira, M. Hanao, and Y. Tsukaguchi: *ISIJ Int.*, 2013, vol. 53, pp. 818–22.
23. H. Nakada and K. Nagata: *ISIJ Int.*, 2006, vol. 46, pp. 441–9.
24. L. Zhou, W. Wang, J. Wei, and B. Lu: *ISIJ Int.*, 2013, vol. 53, pp. 665–72.
25. Y. Cui, L. Wang, J. Yang, J. Zhang, Y. Sasaki, and O. Ostrovski: *Steel Res. Int.*, 2015, vol. 86, pp. 662–9.
26. Y. Kashiwaya, C.E. Cicutti, A.W. Cramb, and K. Ishii: *ISIJ Int.*, 1998, vol. 38, pp. 348–56.
27. Y. Kashiwaya, C.E. Cicutti, and A.W. Cramb: *ISIJ Int.*, 1998, vol. 38, pp. 57–65.
28. W. Wang, K. Blazek, and A. Cramb: *Metall. Mater. Trans. B*, 2008, vol. 39B, pp. 66–74.
29. K. Gu, W. Wang, L. Zhou, F. Ma, and D. Huang: *Metall. Mater. Trans. B*, 2012, vol. 43B, pp. 937–45.
30. A. Badri and A. Cramb: *85th Steelmaking Conference*, Warrendale, PA, 2002.
31. J. Yang, J. Zhang, Y. Sasaki, O. Ostrovski, C. Zhang, D. Cai and Y. Kashiwaya: *Proceedings of the 10th International Conference on Molten Slags, Fluxes and Salts*, TMS, Seattle, 2016.
32. L. Zhou, W. Wang, R. Liu, and B.G. Thomas: *Metall. Mater. Trans. B*, 2013, vol. 44B, pp. 1264–79.
33. A. Dietzel and Z. Elektrochem: *Angew. Phys. Chem.*, 1942, vol. 48, pp. 9–23.
34. J.E. Shelby: *Introduction to Glass Science and Technology*, Royal Society of Chemistry, Cambridge, 2005, p. 14.
35. J. Li, W. Wang, J. Wei, D. Huang, and H. Matsuura: *ISIJ Int.*, 2012, vol. 52, pp. 2220–5.
36. B. Ho: Master thesis, University of Illinois at Urbana-Champaign, 1992.
37. L. Zhou, W. Wang, D. Huang, J. Wei, and J. Li: *Metall. Mater. Trans. B*, 2012, vol. 43B, pp. 925–36.
38. J. Yang, Y. Cui, L. Wang, Y. Sasaki, J. Zhang, O. Ostrovski, and Y. Kashiwaya: *Steel Res. Int.*, 2015, vol. 86, pp. 636–43.
39. T. Watanabe, H. Fukuyama, K. Nagata, and M. Susa: *Metall. Mater. Trans. B*, 2000, vol. 31B, pp. 1273–81.
40. J. Fletcher and F. Glasser: *J. Mater. Sci.*, 1993, vol. 28, pp. 2677–86.
41. J. Kromhout: Doctoral dissertation, Technische Universiteit Delft, 2011.